scientific reports

OPEN

Assessing the accuracy of multi-model approaches for downscaling land surface temperature across diverse agroclimatic zones

Debasish Roy[1], Bappa Das[2], Pooja Singh[3], Priyabrata Santra[4], Shovik Deb[5], Bimal Kumar Bhattacharya[6], Ajit Govind[7], Raghuveer Jatav[1], Deepak Sethi[1], Tridiv Ghosh[1], Joydeep Mukherjee[1], Vinay Kumar Sehgal[1], Prakash Kumar Jha[8], Sheshakumar Goroshi[9], P. V. Vara Prasad[10] & Debashis Chakraborty[1,11]✉

Land surface temperature (LST) is a critical parameter for land surface and atmospheric interactions. However, the applicability of current LST estimates for field-level hydrological, agricultural, and ecological operations is challenging due to their coarse spatiotemporal resolution. In the current article, we compared three different models, namely 1) Thermal Sharpening (TsHARP), 2) Thin Plate Spline (TPS), and 3) Random Forest (RF) for downscaling LST from 100 to 10 m by using high-resolution Sentinel-1,2 optical-microwave data. TsHARP, TPS, and RF are commonly used methods for improving the spatial resolution of large-scale environmental or climate data to finer scales for field-level applications. The analysis was performed at agricultural farms in the semi-arid, arid, and per-humid regions of India during the winter and summer seasons of 2020–21 and 2021–22. The calibration accuracy of the RF model was in better agreement with the coefficient of determination (R^2), root mean square error (RMSE), and normalized RMSE (nRMSE) values ranging between 0.961–0.997, 0.103–0.439 K, and 0.034–0.143%, respectively, and lower values of standard errors for all three locations. Though the validation accuracy of models varied between the regions, RF and TPS consistently outperformed the TsHARP model. Further the impact of individual features on LST downscaling was analyzed using Accumulated Local Effects (ALE) plot. The study concluded that RF is an effective and adaptable strategy that can be used in various agroclimatic zones and land cover types, suggesting its broader applicability in agricultural and ecological operations. Finer resolution LST data with enhanced precision can support tailored field-level decision-making and interventions in agriculture and environmental monitoring.

Keywords TsHARP, TPS, Random forest, Spatial downscaling, Agricultural farm

Land surface temperature (LST) is the skin temperature of the earth's surface, which is required to study processes such as drought[1], monitor spatiotemporal dynamics of urban heat islands[2,3], and the growth status of vegetation[4]. Thermal imaging and retrieval of LST variables from spaceborne sensors are of significant interest in numerous practical applications for remote sensing and the scientific community. LST directs many biophysical processes near the land–atmosphere interface and is a critical component in modeling of surface heat budget[5], soil moisture estimation[6,7], drought and vegetation dynamics[1,4,8,9], forest fire monitoring[10], and geological and geothermal studies[11–13]. Agricultural drought usually leads to reduced crop yields or even crop failure, and is often associated with rising LST and decreased soil moisture[14]. Traditionally, LST was estimated at point locations using radiance measurements from meteorological stations[15,16] but more recent methods rely on thermal remote

[1]ICAR-Indian Agricultural Research Institute, New Delhi 110012, India. [2]ICAR-Central Coastal Agricultural Research Institute, Old Goa, Goa 403402, India. [3]University of California, Davis, CA 95616, USA. [4]ICAR-Central Arid Zone Research Institute, Jodhpur, Rajasthan 342003, India. [5]Uttar Banga Krishi Viswavidyalaya, Cooch Behar, West Bengal 736165, India. [6]Space Applications Centre (ISRO/DOS), Ahmedabad, Gujarat 380015, India. [7]ICARDA, Maadi, Cairo, Egypt. [8]Mississippi State University, Mississippi, MS 39762, USA. [9]India Meteorological Department, New Delhi 110003, India. [10]Department of Agronomy, Kansas State University, Manhattan, KS 66506, USA. [11]International Maize and Wheat Improvement Center (CIMMYT), Dhaka 1212, Bangladesh. ✉email: D.CHAKRABORTY@cgiar.org
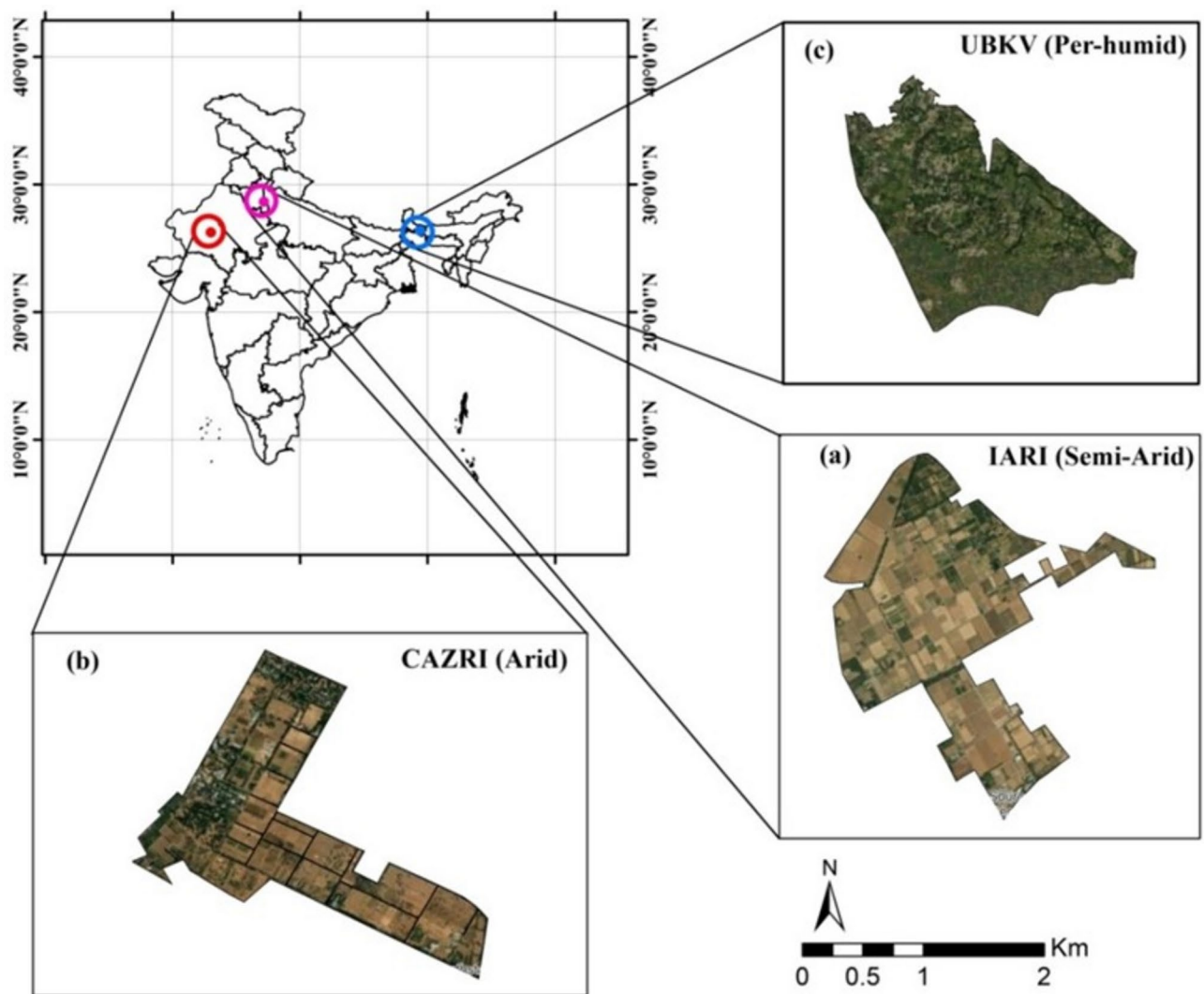
sensing, primarily in the Thermal Infrared (TIR) region, for LST retrieval[17–19]. TIR sensors map the radiation emitted by the earth in a range of 8–15 μm and measure the radiation emitted by the ground to determine the surface temperatures. Satellite-based TIR bands contribute both spatiotemporal coverage at local or global scales and are more cost-efficient and accessible than traditional methods[20]. However, spatial resolutions of satellite-based LST are generally coarse, hindering their use for precise farm-level operations.

The LST highly depends on atmospheric parameters such as relative humidity and near-surface air temperature[21] and sensor parameters like spectral range, viewing geometry, and surface emissivity[22–24]. Due to the high variability of these parameters, satellite-based LST retrieval remains a complex process[25–27]. Many researchers consider atmospheric conditions and Land Surface Emissivity (LSE) as the most important parameters for retrieving LST from remote sensing. The algorithms developed for LST estimation are generally named based on the number of bands used. For example, single-channel or mono-window algorithms use only one thermal band[28,29], whereas split window requires two TIR bands[30]. LST retrieval has been performed using Landsat 5 (TM), Landsat 7 ETM +, and Landsat 8 OLI/TIRS data using Radiative Transfer Equation (RTE), Single Channel Algorithm (SCA) or MWA[31–33].

Current TIR bands has limited applications due to coarser-resolution[34]. Landsat-7/8 provides LST at medium resolution (~100 m) with low temporal frequency (16-day interval), while MODIS offers daily LST at lower spatial resolution (~1000 m). NASA's ASTER provides thermal data at ~90 m with limited access. Therefore, there is a growing interest in enhancing the spatial resolution of LST maps[35]. Spatial downscaling is frequently used to improve the resolution by integrating coarse LST with high-resolution predictor variables[36,37]. Statistics-based models are built on the relationships between LST and other surface characteristics information such as reflectance in the visible, near-infrared (NIR), and shortwave infrared (SWIR) bands, digital elevation model (DEM), and spectral indices available at relatively high spatial resolutions[38,39]. Methods like disaggregation procedure for radiometric surface temperature (DisTrad)[40] and thermal sharpening (TsHARP)[41] are commonly used for this. However, these methods perform poorly in urban and arid regions due to reliance on vegetation variable[42]. TsHARP can downscale coarse thermal images to match the finer resolution of visible and NIR images. It uses the inverse linear relationship between NDVI and LST, making it computationally efficient. However, it may not perform well in areas with mixed vegetation with significant NDVI fluctuation which is inadequately represented by the coarse LST[43]. Under water stress condition also, changes in NDVI are slower than surface temperature changes[7]. The expected inverse linear relationship may not be strong[41,43]. Rawat et al.[44] integrated TsHARP and Thin Plate Spline (TPS) models to downscale LST derived from MODIS thermal imagery from 1 km to 250 m resolution, with good validation against Landsat 7 thermal data. The TPS serves as a powerful and precise deterministic non-geostatistical surface fitting process that adjusts functions to interpolate source point data (coarse LST) while minimizing the smoothness term[45]. Although these models are simplistic in approach, their performance may be limited under complex heterogeneous environments, prompting the use of multi-model or ensemble-based approach for more accurate prediction[46,47].

Machine learning (ML) techniques, leveraging advanced nonlinear methods are being tested for LST downscaling due to their few assumptions, ease of implementation, and ability to handle complex relationships[38,48]. Methods like Artificial Neural Networks (ANN) and Support Vector Machines (SVM) were used for LST and soil moisture retrieval[49]. Three distinct models, namely multiple linear regression (MLR), TsHARP, and random forest (RF) were compared to downscale MODIS LST from 1 km to 100 m[50]. Several ML models were compared for downscaling LST from the 1 km daily MODIS-LST product to 240 m[48]. When validated against LST derived from Landsat-8 thermal imagery, results showed that ML methods outperformed TsHARP. Mustafa et al.[51] used four soft computing techniques, namely, multivariate adaptive regression splines (MARS), wavelet neural networks (WNNs), adaptive neurofuzzy inference systems (ANFIS), and dynamic evolving neurofuzzy inference systems (DENFIS), further demonstrating the potential of ML in improving LST downscaling. A novel LST downscaling technique based on the geographically weighted autoregressive (GWAR) model outperformed TsHARP with respect to RMSE and MAE[52]. A spatial random forest method (SRFD) also utilized various predictor variables, such as land surface reflection, spectral indices, terrain factors, and land cover for improved downscaling[53]. A regression model for urban LST downscaling used the normalized difference built-up index, normalized difference water index, and other remote sensing spectral indices as predictor variables[54]. The impact on the surface urban heat island over different LULC types was analysed using Landsat datasets and graphically weighted regression model (GWR) in semi-arid city, showing a significant association ($R^2 = 0.48$)[55]. The RF model quantified seasonal LST dynamics across different LULC patterns in semi-arid Indian cities[56] while Li et al.[57] downscaled LST using various machine learning methods, including ANN, SVM, and RF, and found that RF outperformed the others. A data driven approach using regression and neural network models has been applied for forecasting urban LST[58]. In a recent study ERA5 LST was downscaled to a 1000 m resolution through pixel-wise temporal alignment iterative linear regression model based on MODIS LST products[59], offering a more stable techniques that preserves the spatial distribution of the ERA5 LST with minimal missing pixels.

Despite significant advancements in remote sensing and downscaling techniques, a comprehensive comparative analysis of various models for LST downscaling over agricultural farms with diverse setting across different agroclimatic zones remains unexplored. In this pretext, the current study aimed to improve the spatial downscaling of LST using three different models, namely TsHARP, TPS, and RF. The proposed study was conducted over three sites located at semi-arid, arid, and per-humid agroclimatic regions (Fig. 1). The objectives of the study were to (1) downscale Landsat 8 TIR-based LST from 100 m resolution to plot level resolution i.e. 10 m; and (2) compare the efficiency of the downscaling models (TsHARP, TPS and RF) over different agroclimatic zones.

Fig. 1. Spatial extent of study areas-(**a**) semi-arid: IARI, New Delhi; (**b**) arid: CAZRI, Jodhpur; and (**c**) per-humid: UBKV, Cooch Behar [Maps were generated using ArcGIS 10.6; https://www.arcgis.com/index.html].

Study areas
Semi-arid, New Delhi (IARI)

The IARI agricultural farm, located in New Delhi (28° 37′ 22.8″ N to 28° 38′ 58.92″ N, 77° 8′ 42.36″ E to 77° 10′ 27.84″ E), spans 242 hectares (Fig. 1a). The soil is coarse to fine loamy in texture. The region has a semi-arid climate with an average annual rainfall of 765 mm, with 82.5% occurring during the southwest monsoon (June to September). The remaining rainfall comes from post-monsoon western disturbances, often bringing cloudy and foggy weather. Dominant crops during winter include wheat, followed by mustard, gram, and lentil.

Arid, Jodhpur (CAZRI)

The CAZRI agricultural farm, located near Jodhpur city in western Rajasthan (26° 15′ 48.38″N to 26° 14′ 26.08″N, 73° 0′ 38.90″E to 72° 59′ 9.99″E), covers 241 hectares (Fig. 1b). The farm's land use is primarily agroforestry, with areas devoted to crops and barren land. The region has an arid climate, characterized by an annual mean temperature of 26.5 °C, average annual rainfall of 500 mm, and potential evapotranspiration (PET) ranging from 1400 to 2000 mm.

Per-humid, Cooch Behar (UBKV)

The UBKV farm and its surrounding area (1045 ha) in Cooch Behar district, West Bengal, India, is located between 26° 23′ to 26° 2′ N and 89° 23′ to 89° 26′ E (Fig. 1c). The region has a humid to per-humid bio-climate, receiving 2400–3700 mm of annual rainfall, with 70% of this occurring during the monsoon season (May to September). The average annual temperatures range from a minimum of 5 °C to a maximum of 37 °C.

Satellite data acquisition

The NASA Landsat-8 (L8) products were acquired from the USGS Earth Explorer (https://ers.cr.usgs.gov). The ESA Level-1 Ground Range Detected (GRD) C-band Synthetic Aperture Radar (SAR) Sentinel-1 data in the Interferometric Wide (IW) swath and Sentinel-2 optical data were acquired from the ESA's Sentinel scientific data hub (https://scihub.copernicus.eu/dhus/#/home). Sentinel-1 products were preprocessed by applying orbit files, thermal and border noise removal, radiometric calibration, speckle filtering using refined Lee filter, Range-Doppler terrain correction using Shuttle Radar Topography Mission (SRTM) DEM. Sentinel-1 data is highly sensitive to vegetation, and soil and plant water contents, establishing an indirect correlation with LST. Consequently, the backscatter coefficient in VV/VH polarization was used for the LST downscaling process. Sentinel-2 Level-2 products provide bottom-of-atmosphere (BOA) reflectance images at 10 and 20 m spatial resolutions and ~ 10 days frequency. We used red, NIR from Operational Land Imager (OLI), and thermal bands (Band 10; Thermal Infrared Sensor, TIRS, 10.6–11.19 μm) for retrieval of LST in this study. For IARI farm, the data were acquired from July 2020 to April 2022, covering both summer and winter seasons. For CAZRI and UBKV farms, only the winter season was covered. A total 75 Level-2 S2 and level-1 L8 cloud-free images were selected for this study. The detail on satellite sensors, data products, and acquisition dates are listed in Supplementary Table S1.

Software tools

The backscatter coefficient in VV/VH polarization was processed using Sentinel Application Platform (SNAP) version 8.0.0. Sentinel-2 bands B2, B3, B4, B8, B11, and B12 were used to calculate 21 vegetation indices using the "spectralIndices" function of the RStoolbox R package[60]. The details about the high-resolution data and the variables are provided in Supplementary Table S2. Landsat-8 has 11 spectral bands in the optical and thermal regions with 30 to 100 m spatial and 16 days temporal resolution. The Level-1 L8 images were corrected atmospherically using the Dark Object Subtraction (DOS) technique with "RStoolbox".

LST retrieval

The LST was retrieved from Landsat-8 band-10 using the Mono Window Algorithm (MWA)[29]. The MWA requires two atmospheric parameters: transmittance and mean atmospheric temperature[61]. The LST was retrieved using the "LST" package[62] in R ver 4.0.2.

Briefly, the digital number (Q_{dn}) was converted to spectral radiance (L_λ, W m^{-2} srad^{-1} μm^{-1}), and then to at-sensor brightness temperature (T_b, Kelvin)[56] by using the Eqs. (1), (2):

$$L_\lambda = M_L \times Q_{dn} + A_L \tag{1}$$

$$T_b = \frac{K_2}{\ln\left(\frac{K_1}{L_\lambda}\right)} \tag{2}$$

where M_L and A_L are the band-specific multiplicative and additive rescaling factors; K_1 (W m^{-2} srad^{-1} μm^{-1}) and K_2 (K) are calibration constants obtained from the metadata file.

LST was derived from at-sensor brightness temperature (T_b, Kelvin) according to Eq. (3):

$$LST = \frac{\{a(1-c-d) + [b(1-c-d)+c+d]T_b - dT_a\}}{c} \tag{3}$$

where a and b are coefficients of a linear function to approximate the derivative of the Planck radiance function[63], c and d are calculated from ground emissivity (ε) and atmospheric transmittance (τ) using Eqs. (4) and (5):

$$c = \varepsilon\tau \tag{4}$$

$$d = (1-\tau)[1+(1-\varepsilon\tau)] \tag{5}$$

ε was estimated using the NDVI-based threshold model[64], while τ was determined from local water vapour content, obtained from near-surface air temperature and relative humidity measured by the automatic weather station (AWS) on the farm. NDVI was calculated using Landsat-8 OLI band 4 (Red, 0.64–0.67 μm) and band 5 (NIR, 0.85–0.88 μm) data. T_a was the effective atmospheric temperature in K, estimated using Eq. (6) [29].

$$T_a = 16.0110 + 0.92621T_0 \tag{6}$$

where T_0 is air temperature at 2 m height.

Atmospheric transmittance (τ) for Landsat-8 band 10 has been calculated using Eq. (7).

$$\tau = -0.0164w^2 - 0.04203w + 0.9715 \tag{7}$$

where w is water vapour content (g/cm^2), computed using Eq. (8).

$$w = 0.0981 \times \left\{10 \times 0.6108 \times \exp\left[\frac{17.27 \times (T_0 - 273.15)}{237.3 + (T_0 - 273.15)}\right] \times RH\right\} + 0.1697 \tag{8}$$

where RH = relative humidity in fraction, and LSE was estimated using NDVI threshold-based method[65,66]

$$\varepsilon = \begin{cases} a - b\rho_{\mathrm{Red}} & NDVI < 0.2 \\ \varepsilon_v P_v + \varepsilon_s \left(1 - P_v\right) + d\varepsilon & 0.2 \le NDVI \le 0.5 \\ \varepsilon_v P_v + d\varepsilon & NDVI > 0.5 \end{cases} \tag{9}$$

where a = 0.973 and b = 0.047 are the empirical constants; ρ_{Red} is the reflectance of the red band; ε_v = 0.973 and ε_s = 0.966 are the emissivity of vegetation and soil, resepctively; P_v is the vegetation proportion given by Eq. (10).

$$\mathrm{P_v} = \left(\frac{\mathrm{NDVI} - \mathrm{NDVI_{min}}}{\mathrm{NDVI_{max}} - \mathrm{NDVI_{min}}} \right)^2 \tag{10}$$

where $\mathrm{NDVI_{min}}$ = 0.2 and $\mathrm{NDVI_{max}}$ = 0.5; $d\varepsilon$ denotes the cavity effect caused by surface roughness (0 for flat surface; otherwise estimated by Eq. (11).

$$d\varepsilon = \left(1 - \varepsilon_s\right)\left(1 - P_v\right) F \varepsilon_v \tag{11}$$

where F is a geometrical shape factor with assumed mean value of 0.55[64].

Downscaling models
Thermal sharpening (TsHARP)
TsHARP model was used to downscale Landsat-8 thermal data at 100 m to 10 m using red and NIR (both at 10 m) reflectance bands obtained from Sentinel-2 (Fig. 2). TsHARP implies that the exclusive relationship exists between LST and VI using RS data at multiple spatial resolutions[45,67]; Eq. (12).
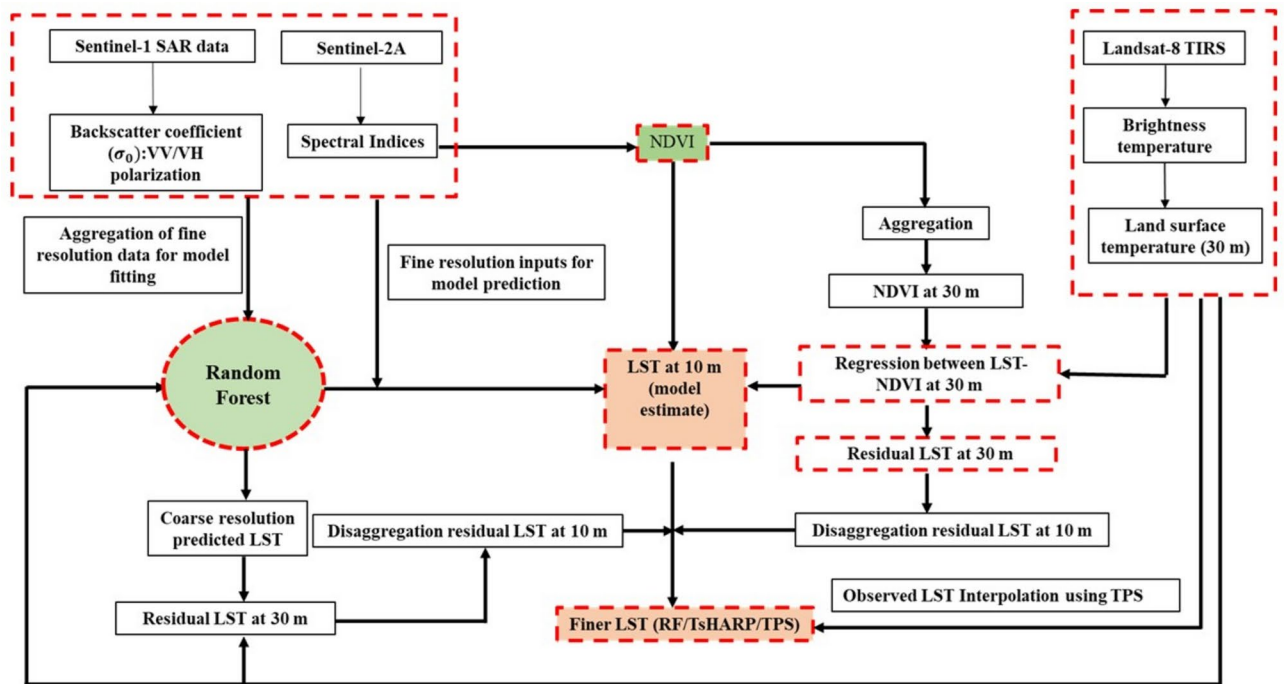
$$LST_{coarse} = a * NDVI_{coarse} + b + \delta_{reg} \tag{12}$$

where LST_{coarse} at 30 m, a and b regression parameters, δ_{reg} - the residual field at 30 m. The regression equation was applied over high-resolution NDVI (10 m), and LST (10 m) as Eq. (13)

$$LST_{fine\_reg} = a * NDVI_{fine} + b \tag{13}$$

Finally, high-resolution LST from TsHARP was obtained by adding residual field (δ_{reg}) behind of regression estimate

$$LST_{TsHARP} = LST_{fine\_reg} + \delta_{reg} \tag{14}$$

Fig. 2. Downscaling methodology of Landsat-8 land surface temperature (LST) at 10 m resolution using RF, TsHARP, and TPS models.

Thin plate spline (TPS)

The fundamental principle of the TPS technique is based on the spatial dependence of geo-data[68]. This method is particularly valuable in scenarios where the primary focus is on spatial continuity and smoothness rather than temporal dynamics.

A general form of the TPS model[69] is represented as Eq. (15):

$$f_{TPS} = a_0 + a_1 x + a_2 y + \sum_{i=1}^{n} b_i r_i^2 log r_i \tag{15}$$

where $r_i^2 = (x - x_i)^2 + (y - y_i)^2$; a_0, a_1, a_2 and b_i are model parameters which are obtained by satisfying Eqs. (16) and (17):

$$f_{low\_TPS} = LST_{coarse} \tag{16}$$

$$LST_{TPS\_high} = f_{high\_TPS} \tag{17}$$

Random forest (RF)

Random forest (RF) is a machine learning technique that constructs an ensemble of decision trees to model complex relationships between high-dimensional input variables and outputs, typically used for both regression and classification[70]. Based on the interpretation of the study region, the 35 foremost drivers of LST were considered for the development RF model (Supplementary Table. S2). The hyperparameters of the RF model were optimized through tenfold cross-validation with 5 repetitions using "caret"[71] and "ranger"[72] packages in R version 4.0.2. Feature selection was performed to eliminate unsuitable variables. It ensures that model training is faster and less complicated, with a higher accuracy[73]. The variable importance for the RF model was computed using the "varImp" function of the "caret" package. For downscaling, the input predictors at fine resolution were first aggregated to match the coarse resolution LST data (equivalent to the ~ 100 m LST of Landsat-8 OLI/TIRS). The statistical relationship between the LST and predictor variables was developed using the RF algorithm:

$$LST_{100m} = f(S_i, \delta_{VV}, \delta_{VH}) \tag{18}$$

where S_i is an ith variable derived from optical data (Sentinel-2A) and δ_{VV}, δ_{VH} are the variables derived from SAR data (Sentinel-1), f is a non-linear function fitted by the random forest[74].

$$\Delta LST_{100m} = LST_{100m} - PLST_{100m} \tag{19}$$

$$PLST_{10m} = PLST_{10m} + \Delta LST_{100m} \tag{20}$$

where $PLST_{100m}$ and $PLST_{10m}$ are predicted LST at 100 and 10 m, ΔLST_{100m} is the residuals at coarse resolution. RF is known for its flexibility in handling large datasets and its ability to account for intricate, non-linear patterns that may not be easily captured by traditional statistical methods.

Accuracy evaluation

Three standard matrices were used to evaluate the model performance namely coefficient of determination (R^2), root means square error (RMSE) and normalised root mean square error (nRMSE) given as:

$$R^2 = \left(\frac{\frac{1}{n} \sum_{i=1}^{n} \left(LST_P - \overline{LST_P} \right) \left(LST_O - \overline{LST_O} \right)}{\sigma_P \sigma_O} \right) \tag{21}$$

$$RMSE = \sqrt{\frac{1}{n} \sum_{i=1}^{n} (LST_P - LST_O)^2} \tag{22}$$

$$nRMSE = \frac{\sqrt{\frac{1}{n} \sum_{i=1}^{n} (LST_P - LST_O)^2}}{\overline{LST_O}} \times 100 \tag{23}$$

LST_P is model output; $\overline{LST_P}$ and σ_P are the mean and standard deviation of model outputs, respectively. LST_O are observations, $\overline{LST_O}$ and σ_O are the mean and standard deviation of observations, respectively. R^2 values close to 1; RMSE close to 0, and lower nRMSE indicate better model performance, as the model's predictions are closer to the actual values. LST derived from Landsat-8 band 10 at 100 m was considered observed LST. This observed LST was downscaled to 10 m resolution using three different models (TsHARP, TPS, and RF). We aggregated the 10 m predicted LST to 100 m for downscaling performance evaluation and compared it with Landsat 8 LST data using statistical indices. For validation, the downscaled LST was further aggregated to 1 km, matching the MODIS LST (MOD11A1 and MYD11A1) in the TIR domain. The downscaled images were resampled to 1000 m using the bilinear interpolation to align with MODIS (1 km resolution).

Sensitivity analysis

Conducting a sensitivity analysis is a crucial step in the pursuit of optimization and enhancing the ML model's predictive capabilities. Accumulated local effects (ALE) plots were used to demonstrate each predictor's impact on LST results, including any nonlinear response. Because ALEs more accurately reflect interactions between predictors, they were used to evaluate main effects rather than conventional partial dependence plots (PDP). The split of training data has an impact on ALE plots, much like it does on VIPs. It is challenging and time-consuming to understand second-order ALE plots, necessitating concurrent evaluation of the main-effect ALE plots. The overall downscaling methodology of Landsat-8 LST data to 10 m spatial resolution is displayed in Fig. 2.

Results

Calibration of RF, TsHARP, and TPS

Results showed that RF and TPS were the best-calibrated models for each agroclimatic zone, followed by TsHARP (Table 1). TPS demonstrated its optimal performance in the arid region (CAZRI), exhibiting high accuracy with R^2, RMSE, and nRMSE values ranging from 0.991 to 0.999, 0.05 to 0.214 K, and 0.018 to 0.069%, respectively. TPS showed the highest mean R^2 (0.993) for the arid zone, while the lowest mean RMSE (0.105 K) and nRMSE (0.035%) were observed for the per-humid region (UBKV). The statistics for TPS remained consistently high across other sites as well. Although TPS performed well by capturing the non-linear relationships with smooth surface fitting, it can be computationally intensive, especially for large datasets. The performance of RF similarly high, with R^2 values ranging from 0.961 to 0.997 for all sites. However, RF generated relatively higher RMSE (0.305–0.439 K) and nRMSE (0.097–0.13%) for the arid site compared to other sites. When all observation dates

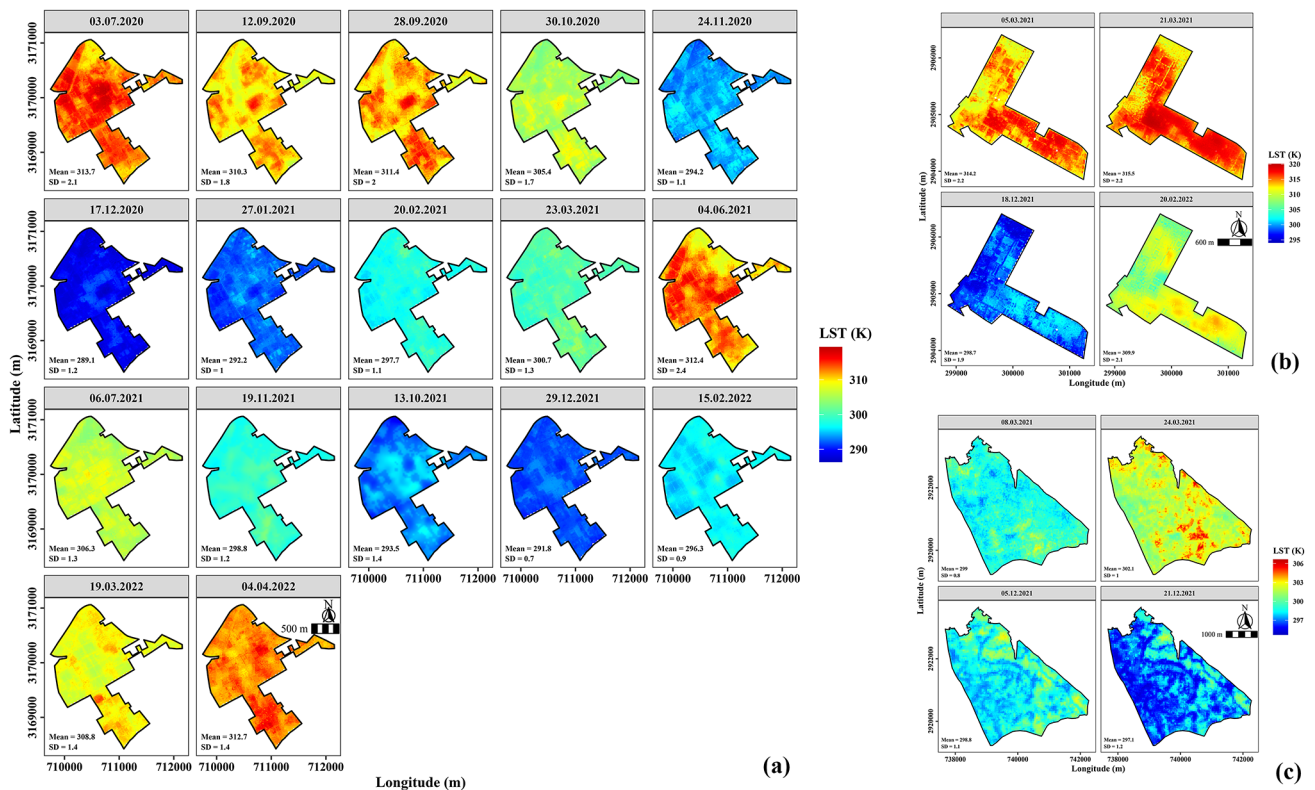| Date	RF			TsHARP			TPS		
	R^2	RMSE (K)	nRMSE (%)	R^2	RMSE (K)	nRMSE (%)	R^2	RMSE (K)	nRMSE (%)
IARI									
30.Oct.2020	0.985	0.228	0.075	0.976	0.367	0.12	0.991	0.176	0.058
24.Nov.2020	0.997	0.196	0.067	0.963	0.276	0.094	0.97	0.227	0.077
17.Dec.2022	0.979	0.192	0.067	0.957	0.256	0.089	0.983	0.173	0.06
27.Jan.2021	0.976	0.163	0.056	0.965	0.166	0.071	0.982	0.143	0.049
20.Feb.2021	0.979	0.173	0.058	0.969	0.233	0.078	0.989	0.129	0.043
23.Mar.2021	0.983	0.192	0.064	0.964	0.309	0.078	0.995	0.106	0.035
18.Nov.2021	0.982	0.167	0.056	0.985	0.165	0.055	0.981	0.174	0.058
13.Dec.2021	0.984	0.186	0.063	0.987	0.173	0.059	0.981	0.204	0.07
29.Dec.2021	0.961	0.153	0.052	0.962	0.161	0.052	0.981	0.204	0.07
15.Feb.2022	0.983	0.142	0.048	0.961	0.233	0.079	0.996	0.069	0.023
19.Mar.2022	0.985	0.187	0.061	0.967	0.312	0.101	0.999	0.045	0.015
04.Apr.2022	0.985	0.187	0.06	0.968	0.292	0.093	0.995	0.11	0.035
Mean	0.982	0.181	0.061	0.969	0.245	0.081	0.987	0.147	0.049
SD	0.008	0.023	0.007	0.009	0.069	0.02	0.009	0.056	0.02
SE	0.0023	0.0065	0.0021	0.0027	0.019	0.0057	0.0024	0.016	0.0056
CAZRI									
5.Mar.2021	0.976	0.385	0.123	0.977	0.359	0.114	0.992	0.214	0.068
21.Mar.2021	0.983	0.305	0.097	0.994	0.17	0.054	0.991	0.213	0.068
18.Dec.2021	0.979	0.323	0.108	0.993	0.178	0.06	0.991	0.205	0.069
21.Feb.2022	0.981	0.439	0.143	0.982	0.274	0.089	0.999	0.055	0.018
Mean	0.98	0.363	0.118	0.987	0.245	0.079	0.993	0.172	0.056
SD	0.003	0.061	0.02	0.008	0.089	0.028	0.004	0.078	0.025
SE	0.0014	0.03	0.0099	0.0041	0.044	0.013	0.0019	0.038	0.012
UBKV									
08.Mar.2021	0.989	0.103	0.034	0.952	0.24	0.08	0.997	0.051	0.017
24.Mar.2021	0.979	0.148	0.049	0.966	0.202	0.067	0.994	0.079	0.026
05.Dec.2021	0.982	0.163	0.054	0.977	0.189	0.063	0.987	0.14	0.047
21.Dec.2021	0.981	0.117	0.06	0.975	0.213	0.072	0.987	0.149	0.05
Mean	0.983	0.133	0.049	0.968	0.211	0.071	0.991	0.105	0.035
SD	0.004	0.028	0.011	0.011	0.022	0.007	0.005	0.047	0.016
SE	0.0021	0.013	0.0055	0.0056	0.01	0.0036	0.0025	0.023	0.008

Table 1. Calibration statistics for downscaled-aggregated land surface temperature using RF, TsHARP and TPS models for semi-arid (IARI), arid (CAZRI) and per-humid (UBKV) regions. R^2 coefficient of determination, *RMSE* root mean square error, *nRMSE* normalized RMSE.

were merged, the RF model outperformed TsHARP and TPS models regarding SD and SE values. The RF model demonstrated good and consistent calibration proficiency in LST downscaling across all three agroclimatic zones, as it is highly robust to overfitting and effective with large datasets. However, it requires comprehensive and large quantities of data, along with careful tuning of hyperparameters, and may lack interpretability in some cases.

Downscaled LST maps at 30 and 10 m spatial resolution

A simultaneous display of downscaled LST maps at 10 m and Landsat-8 LST (the 'reference') at 30 m scales showed similar spatial patterns (Fig. 3; Supplementary Figs. S3–S11). As evident at both resolutions, the LST values effectively captured seasonal temperature trends. At the IARI farm, the image reflected a range of LST values, from as low as 16 °C on December 17, 2020, to as high as 41 °C on July 3, 2020 (Fig. 3a; Supplementary Figs. S3–S5). The reference LST had a fuzzy appearance and was homogeneous in distribution. While the 10 m maps generated by RF and TsHARP appeared similar, the RF maps contained more detailed information, allowing for potential analysis of plot-scale temperature variations and differentiation between crops and adjacent areas. The performance of TPS was comparable to RF (Supplementary Fig. S4). For example, on March 23, 2021, the reference and TPS maps showed a hazy appearance in the north and west parts of IARI farm. In contrast, RF demonstrated superior distinction and clarity. It is important to acknowledge that some indistinctiveness was inherent in both RF and TsHARP methods, necessitating residual correction procedures. During the summer, when noticeable variations in LST occurred across space and time, RF exhibited superior precision compared to the other two methods.

Similarly, over CAZRI, the mean LST values of images were consistent on specific dates across all methods, resembling the reference map (Fig. 3b; Supplementary Figs. S6–S8). The CAZRI farm is diverse in land use and represents a mixed agricultural landscape comprising cropland, agroforestry, pasture, and bare land. The pixels appearing in red indicated high LST values while blue pixels corresponded to low LST. LST maps obtained from the RF and TsHARP methods exhibited similarities and demonstrated the ability to distinguish land use heterogeneity. The reference image had a smoothing effect and was relatively uniform in appearance. The central and southeastern blocks of CAZRI were observed to have higher LST values than the northwestern area, where crops were cultivated. For per-humid UBKV farm, the downscaled LST maps generated by all three models exhibited a homogeneous appearance (Fig. 3c; Supplementary Figs. S9–S11). The farm is predominantly a lowland area with rice crops, where the mean LST varied over a narrow range (24–29 °C). The southeastern block of the farm had a considerably higher LST values (27 °C; March 8, 2021), as it featured orchards, horticultural crops,

Fig. 3. Spatial extent of downscaled land surface temperature (10 m) using the random forest method over (**a**) semi-arid IARI (pre-monsoon to post-monsoon), (**b**) arid CAZRI (post-monsoon) and (**c**) per-humid UBKV (post-monsoon) farms.

rubber plantations intermingled with the rice fields. In contrast, the north-western block, which consisted of low-lying paddy areas, showed comparatively lower values (~ 21 °C) and was more distinguishable in RF maps.
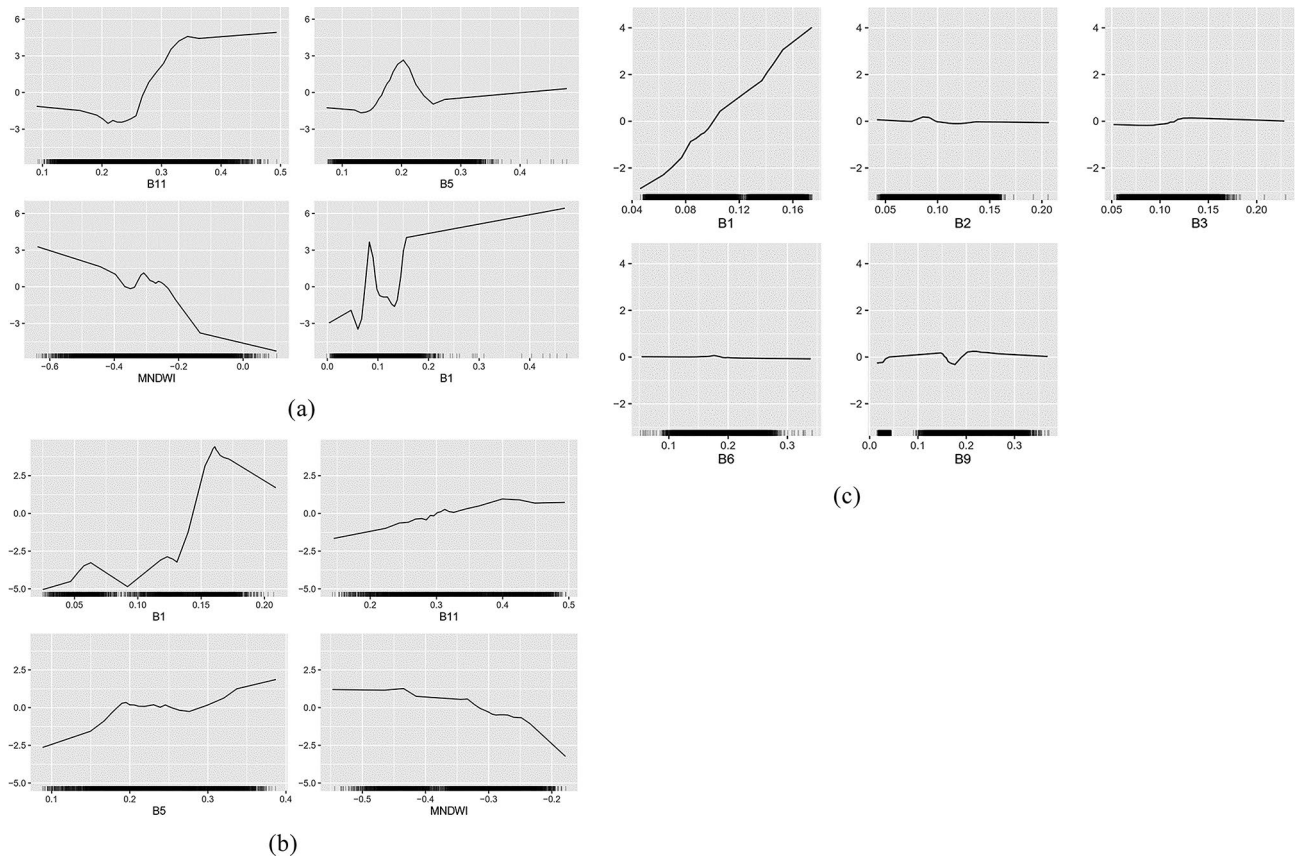
Validation with MODIS data

Since ground-observed LST data was unavailable (use of a thermal camera mounted on a pole in the field for satellite LST validation was not feasible due to significant disagreement between the LST of the camera pixel and the corresponding pixel from the satellite), a comparison was made between 1 km Landsat-8 aggregated LST and the MOD11A1 and MYD11A1 products, both at 1 km spatial resolution. The statistical parameters—R^2, RMSE, and nRMSE obtained for this analysis are presented in Table 2 and Supplementary Fig. S2. Overall, RF provided marginally better predictability in terms of RMSE and nRMSE. The ML approach (RF) and TPS/TsHARP methods showed varied RMSE and nRMSE values for downscaled LST across different dates.

The downscaled aggregated LST followed similar trends to those of MOD11A1 and MYD11A1 LST, although the values were generally underestimated compared to both MODIS Aqua and Terra satellites, with $R^2 = 0.82$ (Aqua) and 0.94 (Terra). However, a significant deviation from the 1:1 line was observed. At the semi-arid site (IARI), RF provided improved model performance, potentially offering up to a 5% improvement over TsHARP and up to a 6% improvement over the TPS model in terms of explained variance, with RMSE between 0.80 and 11.47 K, and nRMSE between 0.27 and 3.84% across all observation dates (Table 2). The R^2, RMSE, and nRMSE for the TsHARP model ranged from 0.39 to 0.93, 0.90 to 11.41 K, and 0.30 to 3.82%, respectively, while for TPS model, the R^2, RMSE, and nRMSE varied from 0.38 to 0.92, 0.90 to 11.41 K, and 0.30 to 3.82%, respectively. It is worth noting that the RMSE values on September 12, 2020, at IARI farm were significantly higher (11.41–11.47 K) for all three downscaling approaches.

At CAZRI, all three models showed substantial agreement (mean $R^2 > 0.84$) between the downscaled and reference LST (Table 2). For the RF model, the R^2 values ranged from 0.75 to 0.91, RMSE from 1.15 to 12.80 K, and nRMSE from 0.36 to 4.30%. For the TPS method, R^2, RMSE, and nRMSE ranged from 0.75 to 0.92, 1.10 to 12.76 K, and 0.35 to 4.29%, respectively. The TsHARP method showed R^2, RMSE, and nRMSE ranging from

Date	RF			TsHARP			TPS		
	R^2	RMSE (K)	nRMSE (%)	R^2	RMSE (K)	nRMSE (%)	R^2	RMSE (K)	nRMSE (%)
IARI									
12.Sep.2020	0.68	11.47	3.84	0.66	11.41	3.82	0.66	11.41	3.82
28.Sep.2020	0.59	6.66	2.18	0.39	6.61	2.17	0.38	6.69	2.16
30.Oct.2021	0.83	4.38	1.45	0.77	4.36	1.45	0.78	4.33	1.44
24.Nov.2020	0.63	3.23	1.09	0.43	3.29	1.11	0.43	3.30	1.11
19.Feb.2021	0.55	1.59	0.53	0.57	1.71	0.57	0.56	1.71	0.57
23.Mar.2021	0.56	5.35	1.75	0.52	5.60	1.83	0.51	5.60	1.83
18.Nov.2021	0.44	1.27	0.43	0.44	1.26	0.42	0.43	1.24	0.42
15.Feb.2022	0.53	0.80	0.27	0.57	0.90	0.30	0.55	0.90	0.30
11.Mar.2022	0.58	1.25	0.57	0.52	2.03	0.68	0.48	2.02	0.68
19.Mar.2022	0.70	2.04	0.66	0.47	2.16	0.70	0.61	2.08	0.68
04.Apr.2022	0.93	6.77	2.26	0.93	6.72	2.2	0.92	6.71	2.19
Mean	0.64	4.07	1.37	0.57	4.18	1.39	0.57	4.18	1.38
SD	4.52	1.24	1.26	3.54	1.31	1.31	3.56	1.31	1.30
SE	1.36	0.37	0.38	1.07	0.40	0.39	1.07	0.39	0.39
CAZRI									
05.Mar.2021	0.88	2.82	0.9	0.88	2.77	0.89	0.88	2.75	0.88
21.Mar.2021	0.75	1.15	0.36	0.75	1.15	0.36	0.75	1.10	0.35
18.Dec.2021	0.91	1.56	0.52	0.89	1.54	0.52	0.92	1.53	0.52
20.Feb.2022	0.85	12.8	4.3	0.85	12.94	4.56	0.84	12.76	4.29
Mean	0.85	4.58	1.52	0.84	4.56	1.52	0.85	4.54	1.51
SD	11.9	0.83	0.82	12.81	0.82	0.81	11.4	0.82	0.81
SE	5.95	0.41	0.41	6.41	0.41	0.41	5.71	0.41	0.40
UBKV									
08.Mar.2021	0.70	0.31	0.11	0.72	0.48	0.16	0.72	0.47	0.16
24.Mar.2021	0.57	3.13	1.05	0.62	3.06	1.03	0.59	3.10	1.04
Mean	0.64	1.72	0.58	0.67	1.77	0.59	0.66	1.78	0.60
SD	7.04	0.86	0.86	9.48	0.97	0.97	6.91	0.96	0.96
SE	4.98	0.61	0.61	6.70	0.69	0.69	4.89	0.68	0.68

Table 2. Validation statistics for downscaled-aggregated land surface temperature with observed LST at 1 km scale using MODIS terra product for semi-arid (IARI), arid (CAZRI) and per-humid (UBKV) regions. *R^2* coefficient of determination, *RMSE* root mean square error, *nRMSE* normalized RMSE.

Fig. 4. Accumulated local effect plots for sensitivity analysis of downscaled land surface temperature using random forest method over (**a**) semi-arid IARI, (**b**) arid CAZRI, and (**c**) per-humid UBKV agricultural farms.

0.75 to 0.89, 1.15 to 12.94 K, and 0.36 to 4.56%, respectively. The RMSE for all three methods was high (12.76—12.94 K) on 20th February 2022 at CAZRI. For the UBKV site, RF displayed R^2 values between 0.57 and 0.70, RMSE between 0.31 and 3.13 K, and nRMSE between 0.11 and 1.05%. Similarly, for TsHARP, the R^2, RMSE, and nRMSE varied between 0.62 and 0.72, 0.48 and 3.06 K, 0.16 and 1.03%, respectively. For the TPS method, R^2 ranged from 0.59 to 0.72, RMSE between 0.47 and 3.10 K, and nRMSE from 0.16 and 1.04%.

Sensitivity analysis results

The variable importance and ALE plot for sensitivity analysis of predictor variables at each experiment site are demonstrated in Supplementary Fig. S1 and Fig. 4, respectively. The trends in variable importance showed consistency between the semi-arid IARI and the arid CAZRI farm. Band 11 (SWIR-1) emerged as the most crucial variable in LST downscaling at both IARI and CAZRI, with subsequent importance assigned to B5, B1, and MNDWI (Fig. 4a and b). These variables had a strong effect on LST prediction. The prediction generally increased with the rising B11 values until the band value reached 0.30 and 0.42 at IARI and CAZRI, respectively. The relationship between prediction and B1 was highly variable, exhibiting both positive and negative associations (0–0.08 and 0.1 onwards at IARI; 0.02–0.06 and 0.15 onwards at CAZRI). MNDWI demonstrated an overall negative effect, implying that higher MNDWI values correspond to lower predictions (Supplementary Fig. S1b).

However, the sensitivity and importance of different parameters varied significantly at the per-humid area (UBKV farm), highlighting the differences in crop types, soil moisture availability, and land use patterns. The coastal aerosol band (B1) was found to be the most critical driver variable in LST downscaling at UBKV (Fig. 4c and Supplementary Fig. S1c). B3, B9, B6, and B2 were among the other top variables significantly affecting the overall LST estimations at UBKV. B9 peaked at 0.2, with both gradual and sharp changes, respectively, exhibiting mixed (positive and negative) effects. Between 0.175 and 0.30 band levels, B6 significantly negatively impacted LST prediction.

Discussion
Downscaling of land surface temperature: comparison of methods

Across three distinct agroclimatic settings, the RF model demonstrated higher sensitivity, distinctly delineating boundaries between agricultural areas, bare soil, and areas with minimal vegetation. The RF model's downscaling of LST to a 10 m resolution captured finer details of the land surface as it incorporated 35 multi-covariates as inputs, ranging from bare to complete vegetation land cover data. Based on the findings of the present study and relevant evidence[75–77], it can be argued that RF makes substantial use of land surface information and exhibits the

relative value of several independent variables, such as the visible, near-infrared (NIR), and shortwave (SWIR) bands. TPS demonstrated exemplary performance in calibration and validation for LST downscaling at all three sites. The findings are consistent with[45,78] which describe TPS as a prominent technique for spatial interpolation of point data sources, making it suitable for complex spatial data. However, despite its accuracy, TPS resulted in some loss of detail in the downscaled LST, as the land surface information was not fully considered during the downscaling process. A major limitation of TPS is its reliance on a sufficiently dense spatial data. It can also struggle with extrapolation beyond the observed range of input variables, which may be problematic in areas with rapidly changing or poorly characterized climatic conditions. Additionally, TPS can be computationally intensive, especially for large datasets.

In contrast to TPS, the linear classical model TsHARP demonstrated the ability to capture clear boundary conditions, particularly for vegetation. TsHARP was applied to downscale ASTER 90 m thermal data to 10 m LST incorporating NDVI derived from Sentinel-2 and achieved satisfactory estimates, especially over vegetated area ($R^2 = 0.853$; RMSE = 0.806 K)[38]. In our study, the calibration accuracy improved significantly, with $R^2 > 0.96$ and RMSE < 0.18 K for all sites. The pixel-wise mean R^2 values of present study ranged between 0.64 and 0.85, which aligns well with the downscaled aggregated LST at 1000 m (MODIS LST) over three agroclimatic zones, matching closely with results obtained by[42,59]. Ebrahimy and Azadbakht[48] evaluated downscaled MODIS-LST product against the LST derived from Landsat-8 thermal imagery using a split window method. The results showed that ML methods outperformed TsHARP models in downscaling LST (with an average RMSE = 2.5 °C) which is comparable to the RMSE found in the present study (1.72–4.58 K). A cross evaluation of high spatial resolution LST (HSR-LST) and Landsat-8 LST values showed highly promising R^2 (0.88–0.97) and RMSE (0.33–0.8 K) values across different cities[79]. The slightly higher error in the current study might be due to the aggregation to MODIS resolution or challenges specific to LST downscaling in heterogeneous landscapes. However, TsHARP exhibited an overestimation of downscaled LST at lower temperatures and an underestimation at higher temperatures, generating errors compared to RF. This inability to anticipate extremely high or low temperatures is typically due to insufficient training data samples[74], although this was unlikely in our study. Hence, it's suggested that models employing global variables should include the entire LST map, as this approach might make conventional models like TsHARP less susceptible to fluctuations in local temperature data. Furthermore, among different land cover types, the predicted LST by TsHARP showed lower accuracy and consistency with reference LST than the RF approach[38,74,80].

Influence of predictor variables on LST downscaling

The SWIR-1 (B11) band was identified as the most sensitive variable for LST downscaling in the relatively drier areas—semi-arid (IARI) and arid (CAZRI). The SWIR reflectance was higher in bare soil with low moisture content, while NIR reflectance was higher in regions dominated by healthy vegetation. Since soil moisture is crucial for maintaining LST, it reliably indicates LST conditions[81,82]. SWIR has proven to be a strong indicator for monitoring SM, especially in semi-arid regions[83] The coastal aerosol band (B1) from Sentinel-2, on the other hand, ranked higher in the per-humid (UBKV) region due to its greater ability to penetrate standing water in rice fields, which is characterized by low-lying topography and flooded conditions for rice (*Oryza sativa*) farming[84,85].

The red edge band (B5) was also identified as one of the critical factors in LST prediction because it can indicate the health status of crops, which in turn controls moisture conditions[86]. The study's findings affirm the effectiveness of the red-edge band in monitoring drought conditions, particularly in areas with bare soil and low vegetation cover. Water-based indices, such as modified normalized difference water index (MNDWI), are also useful for LST downscaling due to their sensitivity to seasonal variations in evaporation, precipitation, moisture content, and air temperature[87]. MNDWI is the modified version of NDWI that uses green and SWIR bands for monitoring water quality and can eliminate the influence of shadow[88].

The SATVI also played an essential role in LST predictions, as it efficiently mapped photosynthesizing biomass and plant litter while compensating for variations in soil brightness and surface conditions. The sigma of vertical-horizontal and vertical–vertical polarization (Sigma0_VH and Sigma0_VV) had significant impacts on LST downscaling, as they are correlated with soil water availability[89,90].

Sources of uncertainties in LST estimation

Three factors primarily contribute to errors in LST estimation[74]. First, spectrum variations resulting from differing acquisition dates of Landsat-8 multispectral, Sentinel-1 SAR, and Sentinel-2 multispectral images (temporal lapse) could introduce inaccuracies. Covariates derived from Sentinel-1, Sentinel-2, and Landsat-8 data exhibited inherent temporal resolution differences, varying by a few days (typically, two to three days earlier or later). These differences may be a primary source of LST downscaling accuracy. Second, aggregating initial (satellite-retrieved) LST data with explanatory factors in the LST retrieval approach may introduce inadvertent errors. Third, residual, an essential strategy for reducing output uncertainty in models, might have introduced additional errors. The bilinear resampling technique used to align the coarse-resolution residual with the downscaled LST was unable to eliminate the model output uncertainty, resulting in certain LST inaccuracies were produced during the residual calibration process.

LST and sustainable development goals

The study on seasonal dynamic changes in LST across different agroclimatic region using an open-source geospatial platform holds significant potential to contribute to multiple sustainable development goals (SDGs). It primarily addresses SDG 2: (Zero Hunger), by providing insights to understanding and addressing challenges related to food production and security. LST provides valuable insights into agricultural water management, resource conservation, and vegetation health, which are essential for achieving SDG 6 (Clean Water and

Sanitation), SDG 13 (Climate Action) benefits from LST data by offering crucial insights for understanding climate trends, assessing vulnerability, and formulating adaptation and mitigation strategies. SDG 15 (Life on Land) used LST as a valuable tool for understanding the health and thermal dynamics of agroecosystems. Plot-level LST data is particularly valuable, such as in precision agriculture, vegetation health monitoring, and urban heat island studies by providing insights into microclimates, soil moisture, and crop stress, which are crucial for targeted management strategies in these fields.

Conclusions

The study evaluated the performance of a ML-based multi-parameter nonlinear regression model (RF) in comparison to a traditional single-parameter-based model (TsHARP) and a non-parameter model (TPS) for downscaling LST (100 m) to a plot level resolution (~ 10 m) using covariates derived from Sentinel-1 and Sentinel- 2 data. The RF model was developed using thirty-five covariates, including optical and SWIR bands, as well as backscatter coefficients, and was calibrated by tuning hyperparameters through tenfold cross-validation for both winter and summer seasons (2020–22). The variable importance analysis, conducted to improve model effectiveness and reduce noise, revealed that B1 (Coastal aerosol) is the most relevant metric for the per-humid region, whereas B11 (SWIR1) band proved crucial parameter for the semi-arid and arid locations. In addition, B3 (green band in Sentinel-2), B5, and water-based index- MNDWI strongly influenced LST downscaling. The RF model provided the best predictability in terms of R^2, RMSE, and nRMSE for semi-arid and per-humid sites, while for the arid region, the performance of TPS was marginally better.

A key limitation of the study that could contribute to errors in LST downscaling was the variation acquisition dates of Landsat-8 multispectral, Sentinel-1 SAR, and Sentinel-2 multispectral images. The findings and methods of this study could contribute to improving the precision and applicability of downscaling techniques for LST, offering valuable insights for monitoring agroecosystems, agricultural water management, resource conservation, and climate trends. By demonstrating the effectiveness of the machine learning-based RF model and comparing its performance with traditional and non-parametric methods, the study provides a robust framework for improving LST resolution to plot level scales.

Data availability

References

1. Wan, Z., Wang, P. & Li, X. Using MODIS land surface temperature and normalized difference vegetation index products for monitoring drought in the southern Great Plains, USA. *Int. J. Remote Sens.* **25**, 61–72 (2004).
2. Nichol, J. Remote sensing of urban heat islands by day and night. *Photogramm. Eng. Remote Sens.* **71**, 613–621 (2005).
3. Huang, X. & Wang, Y. Investigating the effects of 3D urban morphology on the surface urban heat island effect in urban functional zones by using high-resolution remote sensing data: A case study of Wuhan, Central China. *ISPRS J. Photogramm. Remote Sens.* **152**, 119–131 (2019).
4. Julien, Y. & Sobrino, J. A. The Yearly Land Cover Dynamics (YLCD) method: An analysis of global vegetation from NDVI and LST parameters. *Remote Sens. Environ.* **113**, 329–334 (2009).
5. Dutta, D., Gupta, S. & Chakraborty, A. Efefct of different land use land cover on surface head budget-a case study from a tropical humid region of India. *Remote Sens. Appl. Soc. Environ.* **25**, 100675 (2022).
6. Merlin, O., Al Bitar, A., Walker, J. P. & Kerr, Y. An improved algorithm for disaggregating microwave-derived soil moisture based on red, near-infrared and thermal-infrared data. *Remote Sens. Environ.* **114**, 2305–2316 (2010).
7. Sandholt, I., Rasmussen, K. & Andersen, J. A simple interpretation of the surface temperature/vegetation index space for assessment of surface moisture status. *Remote Sens. Environ.* **79**, 213–224 (2002).
8. Casper, M. C. & Vohland, M. Validation of a large scale hydrological model with data fields retrieved from reflective and thermal optical remote sensing data–A case study for the Upper Rhine Valley. *Phys. Chem. Earth Parts A B C* **33**, 1061–1067 (2008).
9. Karnieli, A. et al. Use of NDVI and land surface temperature for drought assessment: Merits and limitations. *J. Clim.* **23**, 618–633 (2010).
10. Maffei, C., Alfieri, S. M. & Menenti, M. Relating spatiotemporal patterns of forest fires burned area and duration to diurnal land surface temperature anomalies. *Remote Sens.* **10**, 1777 (2018).
11. Sekertekin, A. & Arslan, N. Monitoring thermal anomaly and radiative heat flux using thermal infrared satellite imagery–A case study at Tuzla geothermal region. *Geothermics* **78**, 243–254 (2019).
12. Eskandari, A., De Rosa, R. & Amini, S. Remote sensing of Damavand volcano (Iran) using Landsat imagery: Implications for the volcano dynamics. *J. Volcanol. Geotherm. Res.* **306**, 41–57 (2015).
13. Mia, M. B., Fujimitsu, Y. & Nishijima, J. Monitoring of thermal activity at the Hatchobaru-Otake geothermal area in Japan using multi-source satellite images—With comparisons of methods, and solar and seasonal effects. *Remote Sens.* **10**, 1430 (2018).
14. Tarolli, P. & Zhao, W. Drought in agriculture: Preservation, adaptation, migration. *Innov. Geosci.* **1**, 100001–100002 (2023).
15. Becker, F. & Li, Z. Surface temperature and emissivity at various scales: Definition, measurement and related problems. *Remote Sens. Rev.* **12**, 225–253 (1995).
16. Hale, R. C., Gallo, K. P., Tarpley, D. & Yu, Y. Characterization of variability at in situ locations for calibration/validation of satellite-derived land surface temperature data. *Remote Sens. Lett.* **2**, 41–50 (2011).
17. Zhao, W. & Li, Z.-L. Sensitivity study of soil moisture on the temporal evolution of surface temperature over bare surfaces. *Int. J. Remote Sens.* **34**, 3314–3331 (2013).
18. Kamaraj, N. P., Shekhar, S., Sivashankari, V., Balasubramani, K. & Prasad, K. A. Detecting heat-inducing urban built-up surface material with multi remote sensing datasets using reflectance and emission spectroscopy. *Remote Sens. Environ.* **264**, 112591 (2021).

19. Petropoulos, G. P., Srivastava, P. K., Ferentinos, K. P. & Hristopoulos, D. Evaluating the capabilities of optical/TIR imaging sensing systems for quantifying soil water content. *Geocarto Int.* **35**, 494–511 (2020).
20. Gao, C., Tang, B.-H., Wu, H., Jiang, X. & Li, Z.-L. A generalized split-window algorithm for land surface temperature estimation from MSG-2/SEVIRI data. *Int. J. Remote Sens.* **34**, 4182–4199 (2013).
21. Mallick, K. et al. Latent heat flux estimation in clear sky days over Indian agroecosystems using noontime satellite remote sensing data. *Agric. For. Meteorol.* **149**, 1646–1665 (2009).
22. Dash, P., Göttsche, F.-M., Olesen, F.-S. & Fischer, H. Retrieval of land surface temperature and emissivity from satellite data: Physics, theoretical limitations and current methods. *J. Indian Soc. Remote Sens.* **29**, 23–30 (2001).
23. Liu, Y., Yu, Y., Yu, P., Wang, H. & Rao, Y. Enterprise LST algorithm development and its evaluation with NOAA 20 data. *Remote Sens.* **11**, 2003 (2019).
24. Ghent, D. et al. A new approach to defining uncertainties for MODIS land surface temperature. *Remote Sens.* **11**, 1021 (2019).
25. Li, Z.-L. et al. Satellite-derived land surface temperature: Current status and perspectives. *Remote Sens. Environ.* **131**, 14–37 (2013).
26. Trigo, I. F., Monteiro, I. T., Olesen, F. & Kabsch, E. An assessment of remotely sensed land surface temperature. *J. Geophys. Res. Atmos.* https://doi.org/10.1029/2008JD010035 (2008).
27. Cao, B. et al. A review of earth surface thermal radiation directionality observing and modeling: Historical development, current status and perspectives. *Remote Sens. Environ.* **232**, 111304 (2019).
28. Jiménez-Muñoz, J. C. & Sobrino, J. A. A generalized single-channel method for retrieving land surface temperature from remote sensing data. *J. Geophys. Res. Atmos.* https://doi.org/10.1029/2003JD003480 (2003).
29. Qin, Z., Karnieli, A. & Berliner, P. A mono-window algorithm for retrieving land surface temperature from Landsat TM data and its application to the Israel-Egypt border region. *Int. J. Remote Sens.* **22**, 3719–3746 (2001).
30. Yu, X., Guo, X. & Wu, Z. Land surface temperature retrieval from Landsat 8 TIRS—Comparison between radiative transfer equation-based method, split window algorithm and single channel method. *Remote Sens.* **6**, 9829–9852 (2014).
31. Qin Z, Xu B, Zhang W. Li W, Chen Z. Comparison of split window algorithms for land surface temperature retrieval from NOAA-AVHRR data. In *IGARSS 2004. 2004 IEEE International Geoscience and Remote Sensing Symposium*. IEEE, 3740–3743. (2004).
32. Meng, X., Liu, W., Cheng, J., Guo, H. & Yao, B. Estimating hourly land surface temperature from FY-4A AGRI using an explicitly emissivity dependent split-window algorithm. *IEEE J. Sel. Top. Appl. Earth Obs. Remote Sens.* **16**, 5474–5487 (2023).
33. Sekertekin, A. Validation of physical radiative transfer equation-based land surface temperature using Landsat 8 satellite imagery and SURFRAD in-situ measurements. *J. Atmos. Solar Terres. Phys.* **196**, 105161 (2019).
34. Khanal, S., Fulton, J. & Shearer, S. An overview of current and potential applications of thermal remote sensing in precision agriculture. *Comput. Electron. Agric.* **139**, 22–32 (2017).
35. Zhan, W. et al. Disaggregation of remotely sensed land surface temperature: Literature survey, taxonomy, issues, and caveats. *Remote Sens. Environ.* **131**, 119–139 (2013).
36. Atkinson, P. M. Downscaling in remote sensing. *Int. J. Appl. Earth Obs. Geoinf.* **22**, 106–114 (2013).
37. Rathore, P., Prajapati, R., Roy, D., Das, B. & Chakraborty, D. Perspective chapter: Downscaling. In *New Insights Soil-Water Relationship* (eds Datta, R. et al.) (IntechOpen, 2024).
38. Xu, J. et al. Downscaling ASTER land surface temperature over urban areas with machine learning-based area-to-point regression Kriging. *Remote Sens.* **12**, 1082 (2020).
39. Pu, R. & Bonafoni, S. Thermal infrared remote sensing data downscaling investigations: An overview on current status and perspectives. *Remote Sens. Appl. Soc. Environ.* **29**, 100921 (2023).
40. Kustas, W. P., Norman, J. M., Anderson, M. C. & French, A. N. Estimating subpixel surface temperatures and energy fluxes from the vegetation index–radiometric temperature relationship. *Remote Sens. Environ.* **85**, 429–440 (2003).
41. Agam, N., Kustas, W. P., Anderson, M. C., Li, F. & Neale, C. M. U. A vegetation index based technique for spatial sharpening of thermal imagery. *Remote Sens. Environ.* **107**, 545–558 (2007).
42. Pan, X. et al. Applicability of downscaling land surface temperature by using normalized difference sand index. *Sci. Rep.* **8**, 9530 (2018).
43. Lacerda, L. N. et al. Field scale assessment of the tsharp technique for thermal sharpening of modis satellite images using venµs and sentinel-2-derived ndvi. *Remote Sens.* **13**, 1155 (2021).
44. Rawat, K. S., Sehgal, V. K., Singh, S. K. & Ray, S. S. Soil moisture estimation using triangular method at higher resolution from MODIS products. *Phys. Chem. Earth Parts A B C* **126**, 103051 (2022).
45. Rawat, K. S., Sehgal, V. K. & Ray, S. S. Downscaling of MODIS thermal imagery. *Egypt. J. Remote Sens. Sp. Sci.* **22**, 49–58 (2019).
46. Emmerling, J. et al. A multi-model assessment of inequality and climate change. *Nat. Clim. Change* **14**, 1254–1260 (2024).
47. Saini, A. & Sahu, N. Decoding trend of Indian summer monsoon rainfall using multimethod approach: (Century long Indian monsoon rainfall trend). *Stoch. Environ. Res. Risk Assess.* **35**, 2313–2333 (2021).
48. Ebrahimy, H. & Azadbakht, M. Downscaling MODIS land surface temperature over a heterogeneous area: An investigation of machine learning techniques, feature selection, and impacts of mixed pixels. *Comput. Geosci.* **124**, 93–102 (2019).
49. Bindhu, V. M., Narasimhan, B. & Sudheer, K. P. Development and verification of a non-linear disaggregation method (NL-DisTrad) to downscale MODIS land surface temperature to the spatial scale of Landsat thermal data to estimate evapotranspiration. *Remote Sens. Environ.* **135**, 118–129 (2013).
50. Wang, R., Gao, W. & Peng, W. Downscale MODIS land surface temperature based on three different models to analyze surface urban heat island: A case study of Hangzhou. *Remote Sens.* **12**, 2134 (2020).
51. Mustafa, E. K. et al. Study for predicting land surface temperature (LST) using landsat data: a comparison of four algorithms. *Adv. Civ. Eng.* **2020**, 7363546 (2020).
52. Wang, S., Luo, X. & Peng, Y. Spatial downscaling of MODIS land surface temperature based on geographically weighted autoregressive model. *IEEE J. Sel. Top. Appl. Earth Obs. Remote Sens.* **13**, 2532–2546 (2020).
53. Tang, K., Zhu, H. & Ni, P. Spatial downscaling of land surface temperature over heterogeneous regions using random forest regression considering spatial features. *Remote Sens.* **13**, 3645 (2021).
54. Wang, S. et al. Downscaling land surface temperature based on non-linear geographically weighted regressive model over urban areas. *Remote Sens.* **13**, 1580 (2021).
55. Naikoo, M. W., Islam, A. R. M. T., Mallick, J. & Rahman, A. Land use/land cover change and its impact on surface urban heat island and urban thermal comfort in a metropolitan city. *Urban Clim.* **41**, 101052 (2022).
56. Talukdar, S., Naikoo, M. W., Rihan, M., Mohammad, P. & Rahman, A. Seasonal dynamics of land surface temperature and urban thermal comfort with land use land cover pattern in semi-arid Indian cities: Insights for sustainable urban management. *Urban Clim.* **57**, 102105 (2024).
57. Li, W., Ni, L., Li, Z., Duan, S.-B. & Wu, H. Evaluation of machine learning algorithms in spatial downscaling of MODIS land surface temperature. *IEEE J. Sel. Top. Appl. Earth Obs. Remote Sens.* **12**, 2299–2307 (2019).
58. Gupta, N. & Aithal, B. H. Urban land surface temperature forecasting: a data-driven approach using regression and neural network models. *Geocarto Int.* **39**, 2299145 (2024).
59. Wang, N., Tian, J., Su, S. & Tian, Q. A downscaling method based on MODIS product for hourly ERA5 reanalysis of land surface temperature. *Remote Sens.* **15**, 4441 (2023).
60. Leutner B, Horning N, Schwalb-Willmann J, Hijmans RJ. RStoolbox: An R package for remote sensing dataanalysis. *Methods Ecol. Evol.* https://doi.org/10.1111/2041-210X.14451 (2025).

61. Hurtado, E., Vidal, A. & Caselles, V. Comparison of two atmospheric correction methods for Landsat TM thermal band. *Int. J. Remote Sens.* **17**, 237–247 (1996).
62. Das, B., Roy, D., Chakraborty, D. & Rathore, P. LST: Land Surface Temperature Retrieval for Landsat 8. R packageversion 2.0.0. https://CRAN.R-project.org/package=LST (2024).
63. Qin, Z., Dallolmo, G., Karnieli, A. & Berliner, P. Derivation of split window algorithm and its sensitivity analysis for retrieving land surface temperature from NOAA-advanced very high resolution radiometer data. *J. Geophys. Res. Atmos.* **106**, 22655–22670 (2001).
64. Sobrino, J. A., Jiménez-Muñoz, J. C. & Paolini, L. Land surface temperature retrieval from LANDSAT TM 5. *Remote Sens. Environ.* **90**, 434–440 (2004).
65. Sobrino, J. A. & Raissouni, N. Toward remote sensing methods for land cover dynamic monitoring: Application to Morocco. *Int. J. Remote Sens.* **21**, 353–366 (2000).
66. Sobrino, J. A. et al. Land surface emissivity retrieval from different VNIR and TIR sensors. *IEEE Trans. Geosci. Remote Sens.* **46**, 316–327 (2008).
67. Pu, R. Assessing scaling effect in downscaling land surface temperature in a heterogenous urban environment. *Int. J. Appl. Earth Obs. Geoinf.* **96**, 102256 (2021).
68. Chen, X., Li, W., Chen, J., Rao, Y. & Yamaguchi, Y. A combination of TsHARP and thin plate spline interpolation for spatial sharpening of thermal imagery. *Remote Sens.* **6**, 2845–2863 (2014).
69. Keller, W. & Borkowski, A. Thin plate spline interpolation. *J. Geod.* **93**, 1251–1269 (2019).
70. Breiman, L. Random forests. *Mach. Learn.* **45**, 5–32 (2001).
71. Kuhn, M. Building predictive models in R using the caret package. *J. Stat. Softw.* **28**, 1–26 (2008).
72. Wright, MN. & Ziegler, A. ranger : A Fast Implementation of Random Forests for High Dimensional Data in C++and R. *J. Stat. Softw.* **77** https://doi.org/10.18637/jss.v077.i01 (2015).
73. Yan, H. et al. A modification of the bootstrapping soft shrinkage approach for spectral variable selection in the issue of over-fitting, model accuracy and variable selection credibility. *Spectrochim. Acta Part A Mol. Biomol. Spectrosc.* **210**, 362–371 (2019).
74. Hutengs, C. & Vohland, M. Downscaling land surface temperatures at regional scales with random forest regression. *Remote Sens. Environ.* **178**, 127–141 (2016).
75. Xu, N. et al. Changes in the urban surface thermal environment of a Chinese coastal city revealed by downscaling MODIS LST with random forest algorithm. *J. Meteorol. Res.* **35**, 759–774 (2021).
76. Yang, Y. et al. Daily Landsat-scale evapotranspiration estimation over a forested landscape in North Carolina, USA, using multi-satellite data fusion. *Hydrol. Earth Syst. Sci.* **21**, 1017–1037 (2017).
77. Wu, J., Xia, L., On Chan, T., Awange, J. & Zhong, B. Downscaling land surface temperature: A framework based on geographically and temporally neural network weighted autoregressive model with spatio-temporal fused scaling factors. *ISPRS J. Photogramm. Remote Sens.* **187**, 259–272 (2022).
78. Chen, C. & Li, Y. A robust method of thin plate spline and its application to DEM construction. *Comput. Geosci.* **48**, 9–16 (2012).
79. Abunnasr, Y. & Mhawej, M. Fully automated land surface temperature downscaling based on RGB very high spatial resolution images. *City Environ. Interact.* **19**, 100110 (2023).
80. Guo, F., Hu, D. & Schlink, U. A new nonlinear method for downscaling land surface temperature by integrating guided and Gaussian filtering. *Remote Sens. Environ.* **271**, 112915 (2022).
81. Colliander, A. et al. Spatial downscaling of SMAP soil moisture using MODIS land surface temperature and NDVI during SMAPVEX15. *IEEE Geosci. Remote Sens. Lett.* **14**, 2107–2111 (2017).
82. Hulley, G. C. Investigating the effects of soil moisture on thermal infrared land surface temperature and emissivity using satellite retrievals and laboratory measurements. *Remote Sens. Env.* **114**, 1480–1493 (2010).
83. Fensholt, R. & Sandholt, I. Derivation of a shortwave infrared water stress index from MODIS near-and shortwave infrared data in a semiarid environment. *Remote Sens. Environ.* **87**, 111–121 (2003).
84. Brodu, N. Super-resolving multiresolution images with band-independent geometry of multispectral pixels. *IEEE Trans. Geosci. Remote Sens.* **55**, 4610–4617 (2017).
85. Poursanidis, D., Traganos, D., Reinartz, P. & Chrysoulakis, N. On the use of Sentinel-2 for coastal habitat mapping and satellite-derived bathymetry estimation using downscaled coastal aerosol band. *Int. J. Appl. Earth Obs. Geoinf.* **80**, 58–70 (2019).
86. Liu, Y., Qian, J. & Yue, H. Comprehensive evaluation of Sentinel-2 red edge and shortwave-infrared bands to estimate soil moisture. *IEEE J. Sel. Top. Appl. Earth Obs. Remote Sens.* **14**, 7448–7465 (2021).
87. Guha, S. & Govil, H. Relationship between land surface temperature and normalized difference water index on various land surfaces: A seasonal analysis. *Int. J. Eng. Geosci.* **6**, 165–173 (2021).
88. Li, L., Su, H., Du, Q. & Wu, T. A novel surface water index using local background information for long term and large-scale Landsat images. *ISPRS J. Photogramm. Remote Sens.* **172**, 59–78 (2021).
89. Ulaby, F. T., Batlivala, P. P. & Dobson, M. C. Microwave backscatter dependence on surface roughness, soil moisture, and soil texture: Part I-bare soil. *IEEE Trans. Geosci. Electron.* **16**, 286–295 (1978).
90. Das, B. et al. Comparison of bagging, boosting and stacking algorithms for surface soil moisture mapping using optical-thermal-microwave remote sensing synergies. *Catena* **217**, 106485 (2022).

Author contributions

Conceptualization, BKB and DC; Methodology, DR, BD, PR and TG; Formal analysis, BD, RSJ and TG; Investigation, DR, BD, PS, SD, RSJ, DS, JM and VKS; Data collection, RSJ, DS and TG; Resources, PS, SD, AG, JM, VKS, PKJ, PVVP and SG; Writing– original draft, DR, BD and PR; Writing – review & editing, DC, AG and BD; Supervision, DC and BKB; Project administration, DC. All authors have read and agreed to the published version of the manuscript.

Declarations

Competing interests
The authors declare no competing interests.

Additional information
Supplementary Information The online version contains supplementary material available at https://doi.org/10.1038/s41598-025-92135-0.

Correspondence and requests for materials should be addressed to D.C.

Reprints and permissions information is available at www.nature.com/reprints.

Publisher's note Springer Nature remains neutral with regard to jurisdictional claims in published maps and institutional affiliations.